

DuDoNet++ : Encoding mask projection to reduce CT metal artifacts

Yuanyuan Lyu
Z2SKY

Wei-An Lin
UMD

Jingjing Lu
PUMCH

S. Kevin Zhou
ICT

Abstract

CT metal artifact reduction (MAR) is a notoriously challenging task because the artifacts are structured and non-local in the image domain. However, they are inherently local in the sinogram domain. DuDoNet is the state-of-the-art MAR algorithm which exploits the latter characteristic by learning to reduce artifacts in the sinogram and image domain jointly. By design, DuDoNet treats the metal-affected regions in sinogram as missing and replaces them with the surrogate data generated by a neural network. Since fine-grained details within the metal-affected regions are completely ignored, the artifact-reduced CT images by DuDoNet tend to be over-smoothed and distorted. In this work, we investigate the issue by theoretical derivation. We propose to address the problem by (1) retaining the metal-affected regions in sinogram and (2) replacing the binarized metal trace with the metal mask projection such that the geometry information of metal implants is encoded. Extensive experiments on simulated datasets and expert evaluations on clinical images demonstrate that our network called DuDoNet++ yields anatomically more precise artifact-reduced images than DuDoNet, especially when the metallic objects are large.

1. Introduction

Modern computed tomography (CT) systems are able to provide accurate images for diagnosis [21]. However, highly dense objects such as metallic implants lead to severe streaking artifacts, which degrade the image quality of CT and its diagnosis value. Nowadays, with the increasing use of metallic objects and widely adopted low-dose CT, metal artifact reduction (MAR) has become an important problem in CT imaging [23]. During a random survey, Boas *et al.* [3] reported that 48 out of 234 medical scans contained metal artifacts. Compared with normal body tissues, metals have high densities, sharp boundaries, and different attenuation profiles, which lead to severe beam hardening, photon noise, and partial volume artifacts [1, 27, 4]. The contaminated projection data (sinogram) results in non-local artifacts in image domain after reconstruction. The challenge

of MAR aggravates *when the metallic objects are large.*

Conventional MAR algorithms can be grouped into three categories: iterative reconstruction, image domain MAR and sinogram domain MAR. Iterative approaches are often time-consuming and require hand-crafted regularizers, which limit their practical impacts [6, 29, 5, 15, 12]. Image domain methods aim to directly estimate and then remove the streak artifacts from original contaminated image by image processing techniques [28, 17], but they achieve limited success in suppressing artifacts. Sinogram domain methods treat metal-affected regions in sinogram as missing and replace them by interpolation [16, 14] or forward projection [21, 33]. The mismatches in sinogram data after interpolation always result in strong secondary artifacts in the reconstructed image [16, 31, 14]. Forward projection methods first estimate a prior image with various tissue information from the uncorrected image, and then forward project the prior to complete the sinogram [21, 22, 33]. This kind of methods benefit from the clean regions and useful information in corrupted CT image but with strong metal artifacts, the prior estimation errors lead to unfaithful structures. Also, all the sinogram methods would introduce streak artifacts tangent to the metallic objects, as the discontinuity in sinogram is unavoidable.

Recently, convolutional neural networks (CNNs) has been applied to solve MAR [18, 11, 26, 8, 9, 19]. Zhang *et al.* [34] use CNN to generate a prior image from simulated raw and beam-hardening corrected images. Wang *et al.* [30] apply conditional generative adversarial network to learn from paired CT images of pre- and post-cochlear implantation. Gjesteby *et al.* [8] use a deep network to reduce the secondary artifacts after the normalized MAR method [21] with a perceptual loss. Also, lots of efforts have been made to apply CNNs to sinogram completion [7, 23, 10].

While metal artifacts are non-local in the image domain, they are inherently local in the sinogram domain. Aiming to exploit the latter characteristic, the dual domain network (DuDoNet) shown in Figure 1a has been recently proposed to reduce the artifact jointly in sinogram and image domains, which offers advantages over the single domain methods [20]. Specifically, DuDoNet consists of two separate networks, one for sinogram enhancement (SE) and

the other for image enhancement (IE). These two networks are connected by a Radon inversion layer to allow gradient propagation during training. DuDoNet achieves state-of-the-art MAR performance on a large-scale database with simulated metal artifacts.

However, there are still some limitations in DuDoNet [20]. First, in the SE network, a binarized metal trace map is used to indicate the presence of metal in the sinogram. We will theoretically show that such a binarized map is a rather crude representation that *totally discards* the detail inside the metal mask projection. Second, in DuDoNet, the dual domain enhancement is applied on the linearly interpolated sinograms and the correspondingly reconstructed CT. Since linear interpolation only provides a rough estimate to the corrupted sinogram data, the process often results in undesirable secondary artifact, which makes the learning difficult, especially when the metallic implant is large. The artifact reduced images tend to be over-smoothed and severely distorted around regions with high density materials, e.g. bones. Finally, the training data in DuDoNet are simulated by a limited number of projection angles and rays and consequently metal artifact is compounded by strong under-sampling effect.

To address the limitations of DuDoNet [20], we present the DuDoNet++ approach utilizing the realistic information in the original sinogram and image while clearly specifying the metal mask projection. For the SE-Net, instead of using binarized metal trace as input, the SE-Net in the form of U-Net like structure takes the metal mask projection as input and encode it throughout the encoding path in order to best leverage the knowledge of the mask projection. For the IE-Net, rather than using the synthetic image reconstructed from linearly interpolated sinograms, we propose to directly use the metal-affected real image as input. Additionally, it takes the metal mask as input too. Furthermore, we introduce a padding scheme that is designed for sinogram and increase the number of projection angles and rays to avoid the under-sampling effect.

Our contributions are summarized as follows:

- To alleviate the difficulty of enhancing a contaminated sinogram, we use the metal mask projection to guide the restoration. Such a guidance is theoretically justified and brings substantial performance improvement.
- To promote the realism of recovered image, we directly use the metal-affected real image, together with the metal mask, as input to the image enhancement network.
- We boost the MAR performance of DuDoNet by a large margin (over 4dB) on a large-scale database of simulated images. The boost is more evident when the metallic objects are large. Expert evaluations show the effectiveness of our model in clinical scenario.

2. Problem Formulation

2.1. Polychromatic CT imaging model.

CT images represent spatial distribution of linear attenuation coefficients, which indicate the underlying anatomical structure within the human body. Let $X(E)$ denote the linear attenuation image at energy level E . According to Lambert-Beer's Law [2], the ideal projection data (sinogram) S detected by the CT scanner can be expressed as:

$$S = -\ln \int \eta(E) e^{-\mathcal{P}(X(E))} dE, \quad (1)$$

where $\eta(E)$ represents fractional energy at E and \mathcal{P} denotes a forward projection operator. Let x denote a pixel index. $X(E, x)$ can be written as a combination of multiple linear attenuation coefficient of different materials indexed by k ,

$$X(E, x) = \sum_k \lambda_k(E) \rho_k(x), \quad (2)$$

where the mass attenuation coefficient $\lambda_k(E)$ depends on E and k , and $\rho_k(x)$ is the concentration of material k at pixel x . Mass attenuation coefficients of normal body tissue such as water-equivalent component $\lambda_w(E)$ and bone $\lambda_b(E)$ are almost constant with respect to the energy level E , while the mass attenuation coefficient of metal $\lambda_m(E)$ has a large variation. When the metal is absent, let $X = X(E)$, we have $S = \mathcal{P}(X)$. The CT reference image \hat{X} can be reconstructed from the sinogram S by the filtered back projection (FBP) algorithm \mathcal{P}^{-1} : $\hat{X} = \mathcal{P}^{-1}(S)$.

2.2. Metal artifacts.

When the metallic implants are present, $X(E)$ has large variations with respect to E because $\lambda_m(E)$ changes rapidly:

$$X(E) = X_r + X_m(E) = X_r + \lambda_m(E) \rho_m M, \quad (3)$$

where $X_m(E)$ denotes the linear attenuation image of the metallic implants, $X_r = X \odot (1 - M)$ denotes the residual image without the implants, which we want to restore, ρ_m is the density of metal, and M denotes a metal mask,

$$M(x) = \delta[x \in \text{metal}]. \quad (4)$$

where x is a pixel, $\delta[\text{true}] = 1$ and $\delta[\text{false}] = 0$.

According to (2) and the linearity of \mathcal{P} , the forward projection of $X_m(E)$ can be written as:

$$\mathcal{P}(X_m(E)) = \lambda_m(E) \rho_m \mathcal{P}(M) = \lambda_m(E) \rho_m M_p, \quad (5)$$

where $M_p = \mathcal{P}(M)$ is the metal mask projection. Substituting (5) into (1) yields

$$S_{ma} = \mathcal{P}(X_r) - \ln \int \eta(E) e^{-\lambda_m(E) \rho_m M_p} dE. \quad (6)$$

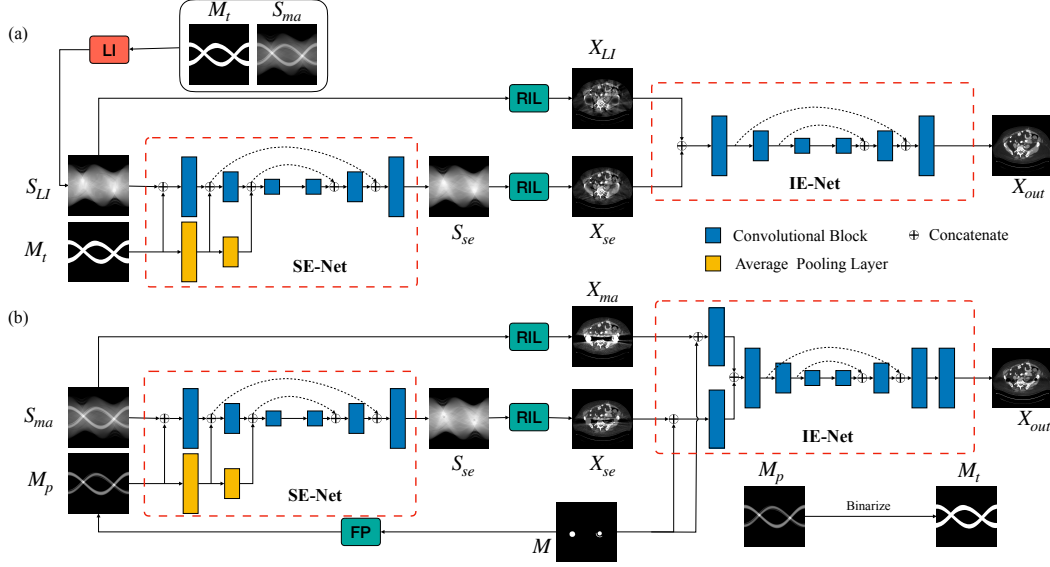


Figure 1. Network architecture. (a) DuDoNet [20]. (b) The proposed DuDoNet++.

It is clear that observed sinogram S_{ma} consists of two terms. The first term $\mathcal{P}(X_r)$ is the projection data originated from X_r . The second term brings metal artifacts. Sinogram domain MAR algorithms aim to restore a clean counterpart S^* (ideally $S^* = \mathcal{P}(X_r)$) from the contaminated sinogram S_{ma} . Then, an artifact-reduced image X^* could be inferred by $\mathcal{P}^{-1}(S^*)$.

3. Proposed Method

To take advantage of the learning from both sinogram and image domains, we use a sinogram enhancement network (SE-Net) and an image enhancement network (IE-Net) to jointly restore a clean image.

3.1. SE-Net.

To restore a clean sinogram from S_{ma} , conventional methods remove the second term in (6) through inpainting. Following this concept, DuDoNet takes linearly interpolated sinogram S_{LI} and binarized metal trace M_t as inputs for sinogram domain enhancement, where

$$M_t = \delta[M_p > 0]. \quad (7)$$

Here, we observe that the second term in (6) is actually a function of M_p . Therefore, we propose to directly *utilize the knowledge of metal mask projection* M_p . Here, SE-Net uses a pyramid U-Net architecture ϕ_{SE} [19], which takes both X_{ma} and M_p as inputs. To retain the projection information, M_p goes through average pooling layers and then fuse with multi-scale feature maps.

We propose a new padding strategy for sinogram data. Since sinogram data is periodic along projection angles,

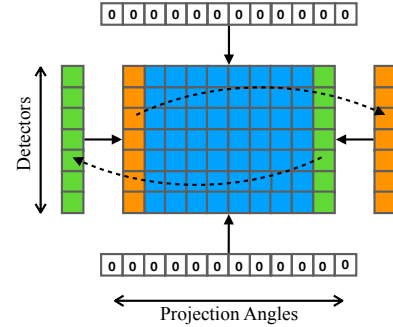


Figure 2. The proposed sinogram padding approach. Periodic padding is applied along the dimension of projection angles. Zero-padding is applied along the dimension of detectors.

we use periodic padding along the direction of projection angles and zero padding along the direction of detectors, as shown in Figure 2. In DuDoNet, zero padding is used in both directions. The new padding strategy can forward more useful information for convolution.

Metals only affect part of the sinogram data of the corresponding projection pathway. To retain the correct sinogram data outside the metal trace, the enhanced sinogram S_{se} is given by a composition of the output of ϕ_{SE} and S_{ma} with respect to M_t :

$$S_{se} = \phi_{SE}(S_{ma}, M_p) \odot M_t + S_{ma} \odot (1 - M_t). \quad (8)$$

We reconstruct the sinogram enhanced image X_{se} by the differentiable Radon Inversion layer (RIL) \mathcal{P}^{-1} first introduced in [20], $X_{se} = \mathcal{P}^{-1}(S_{se})$.

We train ϕ_{SE} with an L_1 loss,

$$\mathcal{L}_{se} = \|S_{se} - S_{gt}\|_1, \quad (9)$$

and use the masked Radon consistency loss to penalize secondary artifact after reconstruction [20],

$$\begin{aligned} \mathcal{L}_{rc} &= \|X_{se} - X_{gt}\|_1 \odot (1 - M) \\ &= \|\mathcal{P}^{-1}(S_{se}) - X_{gt}\|_1 \odot (1 - M). \end{aligned} \quad (10)$$

3.2. IE-Net.

To suppress the secondary artifact in X_{se} , we apply an image enhancement net, which refines X_{se} with M and X_{ma} . The network contains two initial convolutional layers, a U-net [25] and a final convolutional layer. To pay attention to the strongly distorted regions, we concatenate an image (X_{se} or X_{ma}) with metal mask M separately and obtain mask-aware feature maps by an initial convolutional layer with 64×3 kernels. The two sets of mask-aware feature maps are concatenated as the input for the subsequent U-Net. We use a 4-depth U-Net to output a 64-ch feature map. Then, a final convolutional layer outputs the enhanced image X_{out} . To summarize, the whole process can be written as:

$$X_{out} = \phi_{IE}(X_{se}, X_{ma}, M). \quad (11)$$

A masked L_1 loss is used to train ϕ_{IE} :

$$\mathcal{L}_{ie} = \|X_{out} - X_{gt}\|_1 \odot (1 - M). \quad (12)$$

The final loss of our model is:

$$\mathcal{L}_{total} = \alpha_{se}\mathcal{L}_{se} + \alpha_{rc}\mathcal{L}_{rc} + \alpha_{ie}\mathcal{L}_{ie}, \quad (13)$$

where α_{se} , α_{rc} , and α_{ie} are blending weights. We empirically set them to 1.

4. Experiment

4.1. Dataset

Simulation Data. Following [34], degraded S_{ma} and X_{ma} are generated by inserting metallic objects into clean CT image X_{gt} using the metal artifact simulation pipeline with consideration of Poisson noise and partial volume effect. We replace the pixel value of metal mask in X_{gt} with water to obtain sinogram ground truth S_{gt} by forward projection.

We randomly select 4,200 clean CT images from a large scale CT database DeepLesion [32] and use 100 metal masks from [34]. Various metal implants are included, such as dental fillings, spine fixed crews, hip prostheses, coiling and wires, *etc.* We combine 4,000 images with 90 masks for training and 200 images with 10 masks for testing, yielding 360,000 cases for training and 2,000 cases for testing. We

use a fan-beam geometry with 640 uniformly sampled projection angles between 0-360 degree and 641 detector channels per projection angle. The sinogram data have a size of 641×640 . Note that in the original DuDoNet, the sinogram size is 321×320 , which is smaller. The distance from the X-ray source and the rotation center is set to 105.84 cm. For the polychromatic X-ray source, we assume a same spectrum $\eta(E)$ as in [20] and an incident flux photon number of 2×10^7 to simulate Poisson noise. To save GPU memory, we resize all the CT images to 416×416 .

Clinical Data. For testing, given a real clinical metal-affected image X_{ma} , we first segment M base on a threshold of 3000 HU and then obtain the mask projection $M_p = \mathcal{P}(M)$. We assume that X_{ma} is obtained by \mathcal{P}^{-1} of the real S_{ma} . Instead of simulating S_{ma} from a polychromatic projection in [20], we use $\mathcal{P}(X_{ma})$ as a reasonable estimation of S_{ma} since the artifacts related to beam-hardening, Poisson noise and partial volume effect are already present in the real image X_{ma} . We evaluate the proposed method using two clinical datasets. We refer them as DL and CL. DL represents the DeepLesion dataset [32], which includes 928,020 CT images and 32,120 key slices are annotated with representative lesions. CL is a clinical CT scan for a patient with metal rods and screws after spinal fusion. CL is acquired on a GE Discovery CT750 HD scanner with 120 kVp and 275 mAs. We randomly select 30 slices from DL and 10 slices from CL with more than 100 pixels above 3,000 HU and moderate or severe metal artifacts.

4.2. Implementation and Training Details

Our model is implemented using the PyTorch framework [24]. We use the Adam optimizer with $(\beta_1, \beta_2) = (0.5, 0.999)$ to train the model. The learning rate starts from 0.0002, and is halved for every 30 epochs. The model is trained on a Nvidia 2080Ti GPU card with 11 GB RAM for 201 epochs with a batch size of 2.

4.3. Evaluation Methods

Metrics. We use peak signal-to-noise ratio (PSNR) and structural similarity index (SSIM) to evaluate on the corrected image. Compared with neutral images, CT images are presented with a much larger dynamic range of -1024 to +3071 HU. To better quantify the performance for clinical diagnosis, we use a soft tissue window in the range of [-175, +275] HU to compute the metrics. To evaluate the sinogram restoration performance, we use mean square error (MSE) to compare the enhanced S_{se} with S_{gt} . We group results according to the size of metal implants to investigate the MAR performance. The size of the 10 metal masks in the testing set are [32, 53, 111, 115, 115, 242, 448, 878, 879, 2054], and we group every two masks from large to small.

Rating. A proficient radiologist with about 20 years of reading experience is invited to rate the image quality

PSNR(dB)/SSIM%/MSE	Large Metal			→	Small Metal			Average
X_{ma}	19.42/81.1/1.1E+1	23.07/85.4/7.3E+0	26.12/88.7/2.2E+0		26.60/89.3/1.7E+0	27.69/89.9/3.8E-1		24.58/86.9/4.5E+0
IE-Net	31.19/94.8/ n.a.	30.33/95.9/ n.a.	34.48/96.8/ n.a.		35.52/96.8/ n.a.	36.37/97.0/ n.a.		33.58/96.3/ n.a.
SE ₀ -Net	20.28/86.5/3.0E+0	21.65/89.6/1.6E+0	26.39/91.7/3.0E-2		25.65/91.3/6.4E-2	24.93/91.1/8.4E-2		23.78/90.0/9.5E-1
SE-Net	26.71/91.0/2.7E-3	27.93/92.6/4.3E-4	28.20/93.2/2.4E-4		28.31/93.2/1.8E-4	28.34/93.3/1.4E-4		27.90/92.7/7.4E-4
SE _p -Net	26.86/91.0/2.2E-3	27.94/92.5/4.4E-4	28.20/93.1/2.4E-4		28.31/93.2/1.9E-4	28.34/93.3/1.7E-4		27.93/92.6/6.5E-4
SE _p -IE-Net	34.35/96.1/1.7E-3	36.03/96.8/4.4E-4	37.02/97.1/2.4E-4		37.53/97.2/1.9E-4	37.64/97.3/1.5E-4		36.52/96.9/5.5E-4
DuDoNet++	34.60/96.2/3.4E-3	36.84/97.0/4.2E-4	37.84/97.4/2.2E-4		38.34/97.4/1.7E-4	38.38/97.5/1.5E-4		37.20/97.1/8.8E-4

Table 1. Quantitative evaluation for different models.

for each group of the corrected images by paying close attention to ameliorating beam hardening, removing primary streaky artifact, reducing secondary streaky artifacts and overall image quality. With the original metal-affected image on the leftmost, we combine the outputs of different methods in a random order. The radiologist is asked to rate all the images in each group, with a rating from 1, indicating very good MAR performance, to 4, not effective at all. We use paired T-test to compare the ratings between every two methods.

4.4. Ablation Study

In this section, we investigate the effectiveness of different module of proposed architecture. We use the following configurations for this ablation study:

- IE-Net: the IE network with X_{ma} and M ,
- SE₀-Net: the SE network with S_{ma} and M_t ,
- SE-Net: the SE network with S_{ma} and M_p ,
- SE_p-Net: the SE-Net with sinogram padding,
- SE_p-IE-Net: the SE_p-Net with an IE-Net to refine X_{se} with M ,
- DuDoNet++: our full model, SE_p-IE-Net refined with X_{ma} .

Table 1 summarizes all the quantitative results.

Effect of metal mask projection. From Table 1, we can observe the use of M_p instead of M_t improves the performance for at least 4.1 dB in PNSR and reduces MSE from 0.95219 to 0.00074 for all metal sizes. The groups with large metal implants benefit more than groups with small metal implants. As shown in Figure 3, SE₀-Net can not restore the sinogram correctly: the artifacts in metal trace are over-removed or under-removed, which introduces bright and dark bands in the reconstructed CT image. With help of M_p , SE-Net can suppress the artifacts even when the metallic implants are large and the surrogate data are more consistent with the correct data outside the metal trace.

Effect of sinogram padding. From the SE-Net to SE_p-net, we observe sinogram padding mainly improves the performance in the group with largest metal objects, with a

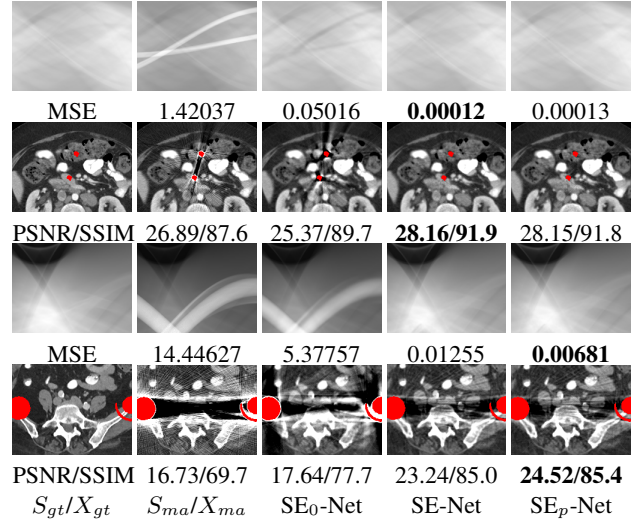


Figure 3. Comparison between different sinogram enhancement networks. Rows 1 and 2 show results on small metallic implants. Rows 3 and 4 show results on large metallic implants. In each case, the enhanced sinograms and the corresponding CT images are presented.

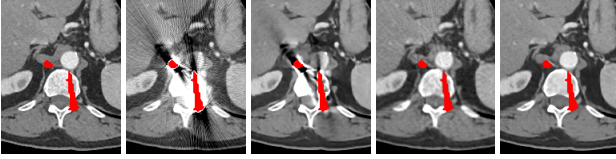
PSNR gain of 0.15 dB and a MSE reduction of 0.00048. Figure 3 demonstrates the model with sinogram padding restores finer details of soft tissue between large metallic objects. The reason is that periodic padding along projection angles retains more correct information than zero-padding.

Effect of dual domain learning. Table 1 shows the performance of the SE_p-IE-Net is much better than the IE-Net (3.0 dB higher) and SEP-Net (9.5 dB higher). Because of the differentiable RIL layer, the sinogram restoration also benefits from dual domain learning with a reduction of 0.0001 in MSE. As shown in Figure 4, the IE-net is capable of removing the small and moderate streak artifacts, but fails to reduce the strong black and bright bands along the projection pathway of metallic objects. the SE_p-Net can suppress most of the artifacts and recover underlying anatomy structure roughly, but secondary artifacts are unavoidable. With dual-domain learning, the SE_p-Net first restore the inconsistent sinogram and then IE-Net remove the new small artifacts.

Effect of learning with X_{ma} . When X_{se} is jointly restored with the corrupted X_{ma} , the sinogram correction per-

PSNR(dB)/SSIM%/MSE	Large Metal		→	Small Metal		Average
X_{ma}	19.42/81.1/1.1E+1	23.07/85.4/7.3E+0	26.12/88.7/2.2E+0	26.60/89.3/1.7E+0	27.69/89.9/3.8E-1	24.58/86.9/4.5E+0
cGAN-CT [30]	16.89/80.7/ n.a.	18.35/83.7/ n.a.	19.94/86.6/ n.a.	21.43/87.6/ n.a.	24.53/89.0/ n.a.	20.23/85.5/ n.a.
LI [16]	20.10/86.7/1.4E-1	22.04/88.7/9.4E-2	25.50/90.2/2.1E-2	26.54/90.7/1.9E-2	27.25/91.2/9.7E-3	24.28/89.5/5.7E-2
NMAR [21]	20.89/86.6/2.3E-1	23.73/89.7/1.3E-1	26.80/91.4/2.7E-2	27.25/91.8/3.6E-2	28.08/92.1/2.2E-2	25.35/90.3/9.0E-2
CNNMAR [34]	23.72/90.1/4.4E-2	25.78/91.6/2.4E-2	28.25/92.6/4.7E-3	28.87/92.9/3.3E-3	29.16/93.1/2.0E-3	27.16/92.0/1.6E-2
Baseline DuDoNet [20]	27.84/92.8/3.3E-2	29.60/94.0/2.7E-2	31.78/94.8/8.7E-3	33.17/95.2/4.9E-3	33.18/95.2/3.7E-3	31.11/94.4/1.5E-2
DuDoNet*	28.98/94.5/5.1E-2	31.00/95.6/3.9E-2	33.80/96.5/5.9E-3	35.61/96.8/3.6E-3	35.67/96.9/2.0E-3	33.01/96.0/2.0E-2
DuDoNet++	34.60/96.2/3.4E-3	36.84/97.0/4.2E-4	37.84/97.4/2.2E-4	38.34/97.4/1.7E-4	38.38/97.5/1.5E-4	37.20/97.1/8.8E-4

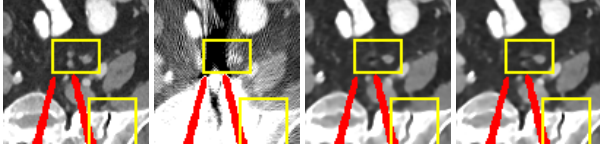
Table 2. Quantitative evaluation for proposed network and the state-of-the-arts methods.



PSNR/SSIM 21.69/84.3 26.26/93.8 26.17/90.7 **34.37/95.0**

X_{gt} X_{ma} IE-Net SE_p -Net SE_p -IE-Net

Figure 4. Comparison of models of single domain and dual-domain enhancement.



PSNR/SSIM 20.36/75.8 33.53/94.4 **34.43/94.7**

X_{gt} X_{ma} SE_p -IE-Net DuDoNet++

Figure 5. Comparison of refinement with and without X_{ma} .

formance is affected with an increment of 0.00033 in MSE, but the overall image quality is improved by 0.7 dB. More details of soft tissue around metal are retained and the image becomes sharper, as shown in Figure 5.

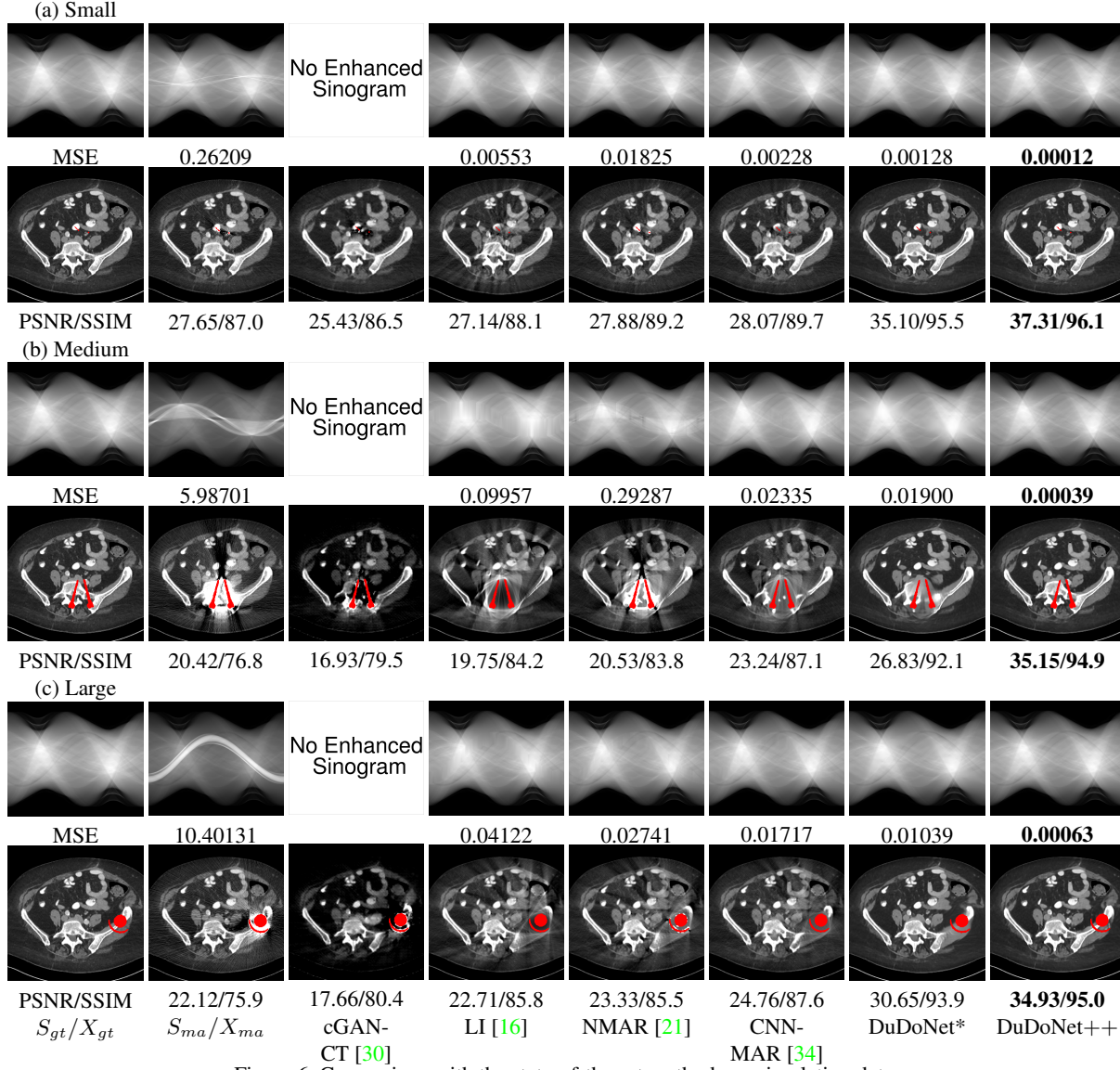
4.5. Comparison on Simulation Data

We compare DuDoNet++ with multiple state-of-the-art MAR methods: LI [16], NMAR [21], cGAN-CT [30], CNNMAR [34], and DuDoNet [20]. LI and NMAR are traditional algorithms, in which we use the simulated S_{ma} as inputs. Wang *et al.* [30] propose conditional GAN for MAR purely in image domain. Here we refer their method as cGAN-CT and retrain the model using pix2pix [13] on our simulation data. For CNNMAR, we use the trained model provided by [34]. Here, the original DuDoNet is retrained on two simulation datasets and supervised with X_{gt} . We refer the model trained on the dataset of [20] with the sinogram resolution (321×320) as Baseline DuDoNet. DuDoNet* denotes the model trained on new simulation data with larger sinogram resolution (641×640).

Quantitative comparisons. Table 2 shows the quantitative comparisons of state-of-the-art methods. Notice that the MSE of DuDoNet is not comparable with other methods because of different geometries and a coarser geometry

makes sinogram inpainting an easier task. We can see all the sinogram domain MAR algorithms outperform image enhancement approach cGAN-CT in PSNR and SSIM. It is because the sinogram restoration only happens inside the metal trace and the correct sinogram data outside the metal trace help to retain the anatomical structure. CNN based methods (CNNMAR, DuDoNet*, DuDoNet++) achieve much better MAR performance than traditional methods, with higher PSNRs and SSIMs in image domain and lower MSEs in sinogram domain. Among all the state-of-the-art methods, CNNMAR achieves the best performance in sinogram enhancement and DuDoNet achieves best performance in reconstructed images. With a finer geometry, DuDoNet* performs better than baseline DuDoNet in PSNR and SSIM. The proposed DuDoNet++ attains the best performance in all metal sizes, with an overall improvement of 4.2 dB in PSNR compared with DuDoNet and 99.4% reduction in MSE compared with CNNMAR.

Visual comparisons. Figure 6 shows visual comparisons in three cases of metallic implants from small to large. For cGAN-CT, when the metallic implants are large, the overall intensity shifts and the soft tissues are not visible in the display window. Sinogram domain or dual domain methods perform much better than cGAN-CT. Figure 6a shows two small metallic implants, we could observe small streaky artifacts tangent to metallic objects and a dark band between metallic objects. All the methods can remove the high intensity metal artifacts in sinogram. Sinogram domain methods (LI, NMAR, CNNMAR) produce stronger secondary artifacts and the reconstructed images get blurred. DuDoNet suppresses all the secondary artifacts through dual domain learning, but the finer details around the smaller metal objects are lost compared with DuDoNet++. As shown in Figure 6b, two spinal rods cause severe streaky artifacts and metal shadows, we could hardly see the bone structures between the two rods. In this case, strong secondary artifacts distort the whole image in LI, NMAR and CNNMAR. In NMAR image, there are fake bone structures around the metals. It is caused by segmentation error in the prior image of strong metal artifacts in corrupted X_{ma} . The segmentation error is also visible in NMAR sinogram. CNNMAR cannot restore the correct



bone structures between rods. The tissues around the rods are over-smoothed in DuDoNet because the sinogram data within metal trace is smooth and lack edge information. The DuDoNet+ image restores the anatomical structures without distortion. Figure 6c considers a hip prosthesis with strong star-like artifacts and white artifacts between the two metal parts. Sinogram domain methods cannot suppress the secondary artifacts and all the other methods fail to recover structures around metallic implants. DuDoNet takes LI sinogram and image as inputs, the missing information cannot be inferred later. DuDoNet++ retains more structural information than DuDoNet, and generates anatomically more faithful artifact-reduced images.

4.6. Clinical Study

Rating. Table 3 summarizes the ratings and P values for comparison between DuDoNet++ and the other methods. The performance of DuDoNet++ is significantly better than cGan-CT, LI, NMAR, CNNMAR on both datasets (all P values ≤ 0.03). DuDoNet++ also achieves better ratings than DuDoNet.

Visual comparisons. Figure 7 shows three clinical CT images with metal artifacts. Case 1 and 2 are with small and moderate metal artifacts. cGan-CT does not suppress the artifacts completely and generate some fake details. LI, NMAR, CNNMAR remove all the artifacts but introduce new streak artifacts, which is caused by the discontinuity in corrected sinogram. DuDoNet outputs over-smoothed sino-

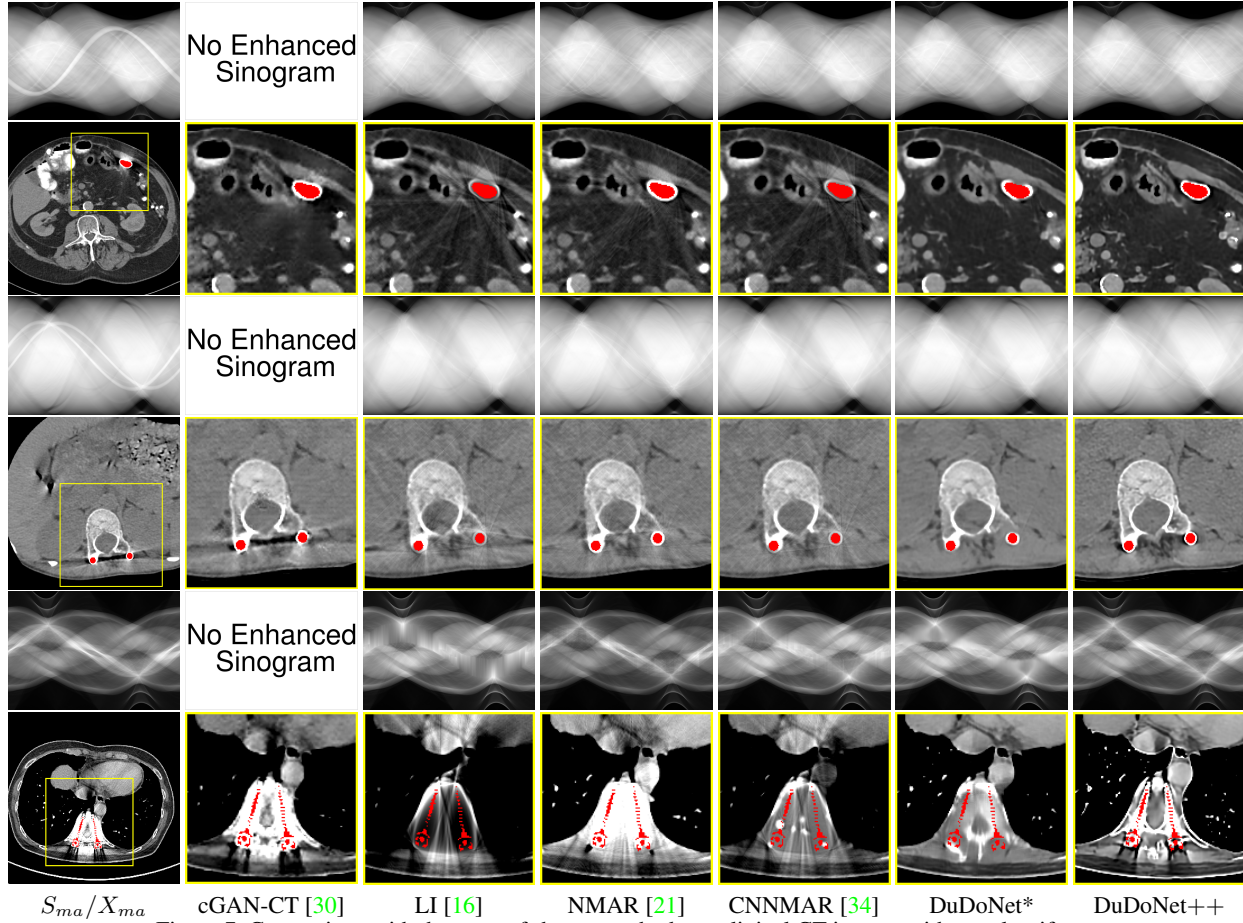


Figure 7. Comparison with the state-of-the-art methods on clinical CT images with metal artifacts.

gram, which causes blurred tissues close to the metal implants, such as muscle and bone. Only DuDoNet++ can provide realistic enhanced sinogram and remove the artifacts while retaining the structure of nearby tissues. Case 3 is very challenging as the rods bring strong metal shadows and bright artifacts around the vertebra. cGan-CT recovers the shape of vertebra but changes the overall image intensity. Other sinogram inpainting methods fail as the soft tissue and bone near the rods are heavily distorted. DuDoNet++ removes part of the dark bands and reproduce correct anatomical structure around the rods.

	DL		CL	
	Rating	P Value	Rating	P Value
cGAN-CT [30]	2.50±0.17	<0.001	4.00±0.00	<0.001
LI [16]	3.80±0.09	<0.001	3.70±0.15	<0.001
NMAR [21]	2.73±0.13	<0.001	2.70±0.15	<0.001
CNNMAR [34]	2.40±0.12	<0.001	2.20±0.20	0.003
DuDoNet*	1.46±0.11	0.312	1.70±0.21	0.278
DuDoNet++	1.27±0.13	n.a.	1.40±0.16	n.a.

Table 3. MAR performance ratings of clinical CT images.

5. Conclusion

In this paper, we present DuDoNet++ to better solve the metal artifact reduction problem. We propose encoding mask projection for the sinogram restoration while utilizing the metal-affected real image and sinogram to retain the rich information in dual domain learning. With the fine details recovered in metal trace, our model can correctly restore the underlying anatomical structure even with large metallic objects. Visual comparisons and qualitative evaluations demonstrate that DuDoNet++ yields better image quality than competing approaches and shows great potential of reducing metal artifacts even when applied to clinical images. In future, we plan to conduct a large scale clinical study to thoroughly evaluate the DuDoNet++ approach in real clinical practices.

References

- [1] J. F. Barrett and N. Keat. Artifacts in ct: recognition and avoidance. *Radiographics*, 24(6):1679–1691, 2004. 1
- [2] Beer. Bestimmung der absorption des rothen lights in farbigen flssigkeiten. *Annalen der Physik*, 162(5):78–88, 1852. 2
- [3] F. E. Boas and D. Fleischmann. Evaluation of two iterative techniques for reducing metal artifacts in computed tomography. *Radiology*, 259(3):894–902, 2011. 1
- [4] F. E. Boas and D. Fleischmann. Ct artifacts: causes and reduction techniques. *Imaging in Medicine*, 4(2):229–240, 2012. 1
- [5] Z. Chang, D. H. Ye, S. Srivastava, J.-B. Thibault, K. Sauer, and C. Bouman. Prior-guided metal artifact reduction for iterative x-ray computed tomography. *IEEE transactions on medical imaging*, 38(6):1532–1542, 2018. 1
- [6] I. A. Elbakri and J. A. Fessler. Segmentation-free statistical image reconstruction for polyenergetic x-ray computed tomography. In *Proceedings IEEE International Symposium on Biomedical Imaging*, pages 828–831. IEEE, 2002. 1
- [7] M. U. Ghani and W. C. Karl. Fast enhanced ct metal artifact reduction using data domain deep learning. *IEEE Transactions on Computational Imaging*, 2019. 1
- [8] L. Gjestebj, H. Shan, Q. Yang, Y. Xi, B. Claus, Y. Jin, B. De Man, and G. Wang. Deep neural network for ct metal artifact reduction with a perceptual loss function. In *Proceedings of The Fifth International Conference on Image Formation in X-ray Computed Tomography*, 2018. 1
- [9] L. Gjestebj, Q. Yang, Y. Xi, B. Claus, Y. Jin, B. De Man, and G. Wang. Reducing metal streak artifacts in ct images via deep learning: Pilot results. In *The 14th international meeting on fully three-dimensional image reconstruction in radiology and nuclear medicine*, volume 14, pages 611–614, 2017. 1
- [10] L. Gjestebj, Q. Yang, Y. Xi, Y. Zhou, J. Zhang, and G. Wang. Deep learning methods to guide ct image reconstruction and reduce metal artifacts. In *Medical Imaging 2017: Physics of Medical Imaging*, volume 10132, page 101322W. International Society for Optics and Photonics, 2017. 1
- [11] H. Gupta, K. H. Jin, H. Q. Nguyen, M. T. McCann, and M. Unser. Cnn-based projected gradient descent for consistent ct image reconstruction. *IEEE transactions on medical imaging*, 37(6):1440–1453, 2018. 1
- [12] B. Hamelin, Y. Goussard, D. Gendron, J.-P. Dussault, G. Cloutier, G. Beaudoin, and G. Soulez. Iterative ct reconstruction of real data with metal artifact reduction. In *2008 5th IEEE International Symposium on Biomedical Imaging: From Nano to Macro*, pages 1453–1456. IEEE, 2008. 1
- [13] P. Isola, J.-Y. Zhu, T. Zhou, and A. A. Efros. Image-to-image translation with conditional adversarial networks. In *Proceedings of the IEEE conference on computer vision and pattern recognition*, pages 1125–1134, 2017. 6
- [14] K. Y. Jeong and J. B. Ra. Reduction of artifacts due to multiple metallic objects in computed tomography. In *Medical Imaging 2009: Physics of Medical Imaging*, volume 7258, page 72583E. International Society for Optics and Photonics, 2009. 1
- [15] P. Jin, C. A. Bouman, and K. D. Sauer. A model-based image reconstruction algorithm with simultaneous beam hardening correction for x-ray ct. *IEEE Transactions on Computational Imaging*, 1(3):200–216, 2015. 1
- [16] W. A. Kalender, R. Hebel, and J. Ebersberger. Reduction of ct artifacts caused by metallic implants. *Radiology*, 164(2):576–577, 1987. 1, 6, 7, 8
- [17] S. Karimi, H. Martz, and P. Cosman. Metal artifact reduction for ct-based luggage screening. *Journal of X-ray science and technology*, 23(4):435–451, 2015. 1
- [18] H. Lee, J. Lee, and S. Cho. View-interpolation of sparsely sampled sinogram using convolutional neural network. In *Medical Imaging 2017: Image Processing*, volume 10133, page 1013328. International Society for Optics and Photonics, 2017. 1
- [19] H. Liao, W.-A. Lin, Z. Huo, L. Vogelsang, W. J. Sehnert, S. K. Zhou, and J. Luo. Generative mask pyramid network for ct/cbct metal artifact reduction with joint projection-sinogram correction. In *International Conference on Medical Image Computing and Computer-Assisted Intervention*, pages 77–85. Springer, 2019. 1, 3
- [20] W.-A. Lin, H. Liao, C. Peng, X. Sun, J. Zhang, J. Luo, R. Chellappa, and S. K. Zhou. Dudonet: Dual domain network for ct metal artifact reduction. In *Proceedings of the IEEE Conference on Computer Vision and Pattern Recognition*, pages 10512–10521, 2019. 1, 2, 3, 4, 6
- [21] E. Meyer, R. Raupach, M. Lell, B. Schmidt, and M. Kachelrieß. Normalized metal artifact reduction (nmar) in computed tomography. *Medical physics*, 37(10):5482–5493, 2010. 1, 6, 7, 8
- [22] J. Müller and T. M. Buzug. Spurious structures created by interpolation-based ct metal artifact reduction. In *Medical Imaging 2009: Physics of Medical Imaging*, volume 7258, page 72581Y. International Society for Optics and Photonics, 2009. 1
- [23] H. S. Park, Y. E. Chung, S. M. Lee, H. P. Kim, and J. K. Seo. Sinogram-consistency learning in ct for metal artifact reduction. *arXiv preprint arXiv:1708.00607*, 2017. 1
- [24] A. Paszke, S. Gross, S. Chintala, G. Chanan, E. Yang, Z. DeVito, Z. Lin, A. Desmaison, L. Antiga, and A. Lerer. Automatic differentiation in pytorch. 2017. 4
- [25] O. Ronneberger, P. Fischer, and T. Brox. U-net: Convolutional networks for biomedical image segmentation. In *International Conference on Medical image computing and computer-assisted intervention*, pages 234–241. Springer, 2015. 4
- [26] M. Sakamoto, Y. Hiasa, Y. Otake, M. Takao, Y. Suzuki, N. Sugano, and Y. Sato. Automated segmentation of hip and thigh muscles in metal artifact-contaminated ct using convolutional neural network-enhanced normalized metal artifact reduction. *arXiv preprint arXiv:1906.11484*, 2019. 1
- [27] R. Schulze, U. Heil, D. Groß, D. Bruellmann, E. Dranischnikow, U. Schwanecke, and E. Schoemer. Artefacts in cbct: a review. *Dentomaxillofacial Radiology*, 40(5):265–273, 2011. 1
- [28] H. Soltanian-Zadeh, J. P. Windham, and J. Soltanianzadeh. Ct artifact correction: an image-processing approach. In

Medical Imaging 1996: Image Processing, volume 2710, pages 477–485. International Society for Optics and Photonics, 1996. [1](#)

- [29] G. Wang, D. L. Snyder, J. A. O’Sullivan, and M. W. Vannier. Iterative deblurring for ct metal artifact reduction. *IEEE transactions on medical imaging*, 15(5):657–664, 1996. [1](#)
- [30] J. Wang, Y. Zhao, J. H. Noble, and B. M. Dawant. Conditional generative adversarial networks for metal artifact reduction in ct images of the ear. In *International Conference on Medical Image Computing and Computer-Assisted Intervention*, pages 3–11. Springer, 2018. [1](#), [6](#), [7](#), [8](#)
- [31] J. Wei, L. Chen, G. A. Sandison, Y. Liang, and L. X. Xu. X-ray ct high-density artefact suppression in the presence of bones. *Physics in Medicine & Biology*, 49(24):5407, 2004. [1](#)
- [32] K. Yan, X. Wang, L. Lu, L. Zhang, A. P. Harrison, M. Bagheri, and R. M. Summers. Deep lesion graphs in the wild: relationship learning and organization of significant radiology image findings in a diverse large-scale lesion database. In *Proceedings of the IEEE Conference on Computer Vision and Pattern Recognition*, pages 9261–9270, 2018. [4](#)
- [33] Y. Zhang, H. Yan, X. Jia, J. Yang, S. B. Jiang, and X. Mou. A hybrid metal artifact reduction algorithm for x-ray ct. *Medical Physics*, 40(4):041910, 2013. [1](#)
- [34] Y. Zhang and H. Yu. Convolutional neural network based metal artifact reduction in x-ray computed tomography. *IEEE Transactions on Medical Imaging*, 37(6):1370–1381, June 2018. [1](#), [4](#), [6](#), [7](#), [8](#)